PROCEEDINGS, 43rd Workshop on Geothermal Reservoir Engineering
Stanford University, Stanford, California, February 12-14, 2018
SGP-TR-213

3D Imaging from vertical DAS fiber at Brady's Natural Laboratory

Whitney TRAINOR-GUITTON[1], Antoine GUITTON[2,1], Samir JREIJ[1], Hayden POWERS[1], C. Bane SULLIVAN[1], James SIMMONS[1], PoroTomo Team

[1]Dept. of Geophysics, Colorado School of Mines, 1500 Illinois St., Golden, CO 80401

[2]DownUnder Geosolutions, Denver, CO

wtrainor@mines.edu

Keywords: distributed acoustic sensing, depth migration, faults, modeling, Born, converted waves

ABSTRACT

Faults play an important role in geothermal fluid transport and can also present a contrast in acoustic impedance such that seismic methods can approximately locate their presence in the subsurface. Brady's Natural Lab is a geothermal reservoir that has numerous faults that allow for deep-to-shallow heat exchange via subsurface fluids. In March 2016 at Brady's, a continuous active seismic survey collected 184 three-component shots, while a vertical DAS cable was in place 150 to 280 meters below surface.

Forward modeling was performed to understand the volume of illumination given the location of the vertical DAS cable and the geometry of the vibe shots. Reverse time migration (RTM), a prestack depth migration method, was used. The modeling domain is 1,560m by 915m by 1,500m in x, y and z respectively. First, four horizontal reflectors (by inserting two constant velocity layers) that extended through the entire modeling domain, ranging in depths of 750m to 1,300m, were used demonstrate which locations in the image are reliable and not migration artifacts, using the most current velocity model for the area. Next, imaging of the current fault model of Brady's was performed to analyze if certain fault dips and strikes would be detectable given the shot geometry. The observed (field) and synthetic data demonstrate the importance of shear wave mode conversions; the vertical DAS fiber is sensitive to particle motion along the cable. For some azimuths, the steeply dipping faults produce reflected shear waves that propagate close to a perpendicular angle of incidence relative to the fiber thus with particle motion parallel to the fiber. The final reflectivity model indicated faults passing through the well and as far away as 800m (from the wellhead) can be imaged with well-processed data, assuming the velocity model is accurate.

Finally, the real data were migrated to analyze the resolving power of the DAS cable. Bright spots exist that are consistent with three faults: the fault farthest from the DAS well at distance of ~750m to the northeast, and two Western-dipping faults below the well that contains the DAS. This confirms how valuable forward modeling using a priori information (here the fault geometry) is to understand how the shot density and locations will illuminate the fault locations. Future work will focus on the shear waves generated by the horizontal vibrators (inline and crossline) which exist at each shotpoint location from the Brady's March 2016 acquisition.

1. INTRODUCTION

Distributed acoustic sensing (DAS) has been used in the oil and gas industry along with and in place of geophones, as it provides denser spatial sampling than geophones (Mateeva et al., 2014; Daley et al., 2016). Countering the increased spatial resolution, however, is DAS's lower signal-to-noise ratio due to imperfect fiber-subsurface coupling and the $\cos^2\theta$ directionality sensitivity (where θ is the angle of incidence of the wave to the DAS fiber). The coupling of the fiber downhole can vary depending on if the fiber is installed behind casing or in tubing (Raterman et al., 2017).

1.1 Vertical DAS data from the Brady Experiment March 2016

In March 2016, a four-week experiment was performed at Brady's Natural Lab, where Ormat Technologies has maintained a geothermal resource and operated a power plant for approximately 25 years. The variety of seismic, geodetic (InSAR), and hydraulic (injection and pumping) activities and/or data collected are described in detail in Feigl et al. (2017). Of greater importance for this work, a vibrating source named T-REX injected the 3 modes (P, transverse S, and longitudinal S) at 191 source locations during each of the four stages of the 15-day field experiment. The four stages describe different production and injection regimes performed during the experiment: 1) normal production/injection, 2) production/injection stopped, 3) increased injection and pulsing production and 4) normal production/injection. The vibroseis truck operated in synchronization with the DAS array and the conventional seismometers. For each of the three modes, the vibroseis source made three sweeps over 20 seconds. Each sweep increased in frequency from 5 Hz to 80 Hz. To record the reflected and diffracted energy from these sources, there were 238 5Hz 3-component geophones, 8,700 meters of horizontal DAS cable (buried in a shallow trench) and 400 meters of DAS cable hanging vertically in Well 56-1 (Figure 1).

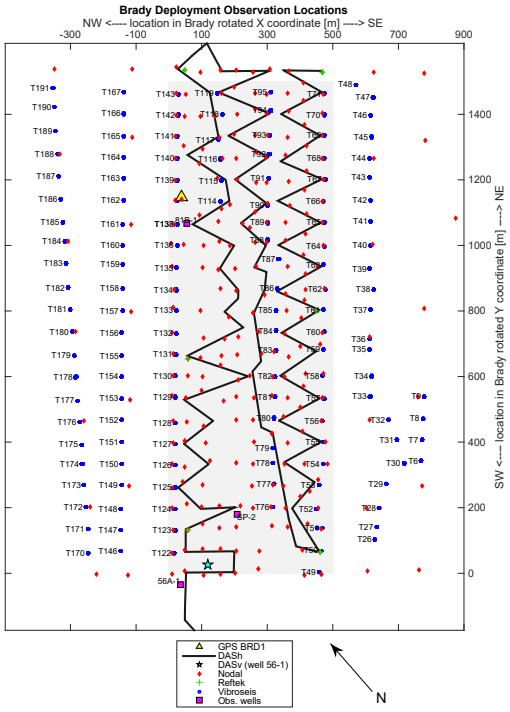

Figure 1: PoroTomo Survey with Seismic Vibe Points (shots) shown in blue (numbers labeled). Well 56-1 with vertical DAS is green star (bottom center). Horizontal DAS in solid black line.

Geologic faults of Brady's (located near Fernley, Nevada) have been studied extensively (Coolbaugh et al., 2004; Faulds et al., 2010; Siler and Faulds, 2013), as it is interpreted that they provide one of the principal means for recharge of the geothermal reservoir (Feigl et al., 2017). Queen et al. (2016) concluded that vertical seismic profiling would be more successful than surface sensors at imaging the nearly vertical faults expected at Brady's. In particular, Siler and Faulds (2013) provided a 3D numerical fault model for the Brady's system. Figure 2 shows the five major faults from the Siler model, the position of Well 56-1, and the shot locations in green. The local PoroTomo coordinate system, seen in Figure 2, was chosen such that the Y axis is oriented along the major fault strikes. Note the three labeled faults in Figure 2, as they are highlighted when comparing the imaging from the synthetic and field data in Section 4.

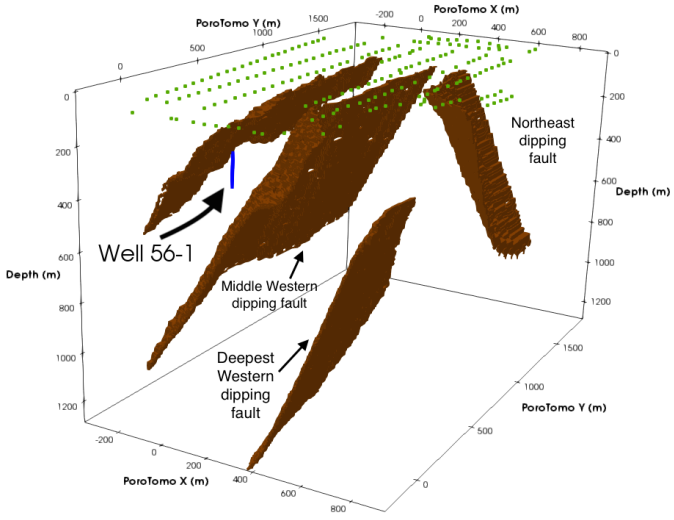

Figure 2: Southern view of 3D rendering of 5 fault model. Well 56-1A (location of vertical DAS) and surface sources shown in green dots). Additionally, the 3 faults successfully imaged and described in Section 4 are labeled: middle & deepest Western dipping fault on the left and the Northeast dipping fault on the right.

Specifically, this paper focuses on understanding the vertical DAS (DASV) data and the extent to which DASV can be used for imaging of the steeply dipping faults. The DASV have potential to be more sensitive to the faults than the horizontal DAS and surface geophones, which are prone to spatial aliasing (Jreij et al., 2018). However, DASV are only recorded in Well 56-1 location, and unfortunately, the fiber is not securely coupled to the casing but is handing freely (Feigl et al., 2017).

Figure 3 shows examples of the DASV data from two different shot points (vibe locations 125 and 199) that are at equivalent offset, but demonstrate the azimuthal heterogeneity of the subsurface. Both are from p-mode sources during stage 3 (time interval) and thus denoted by "30125" and "30199". Figure 3a is for shot point 30125 which is about 257 meters to the northwest of Well 56-1, and Figure 3b shows shot point 30199 located 256 meters to the southwest.

a)

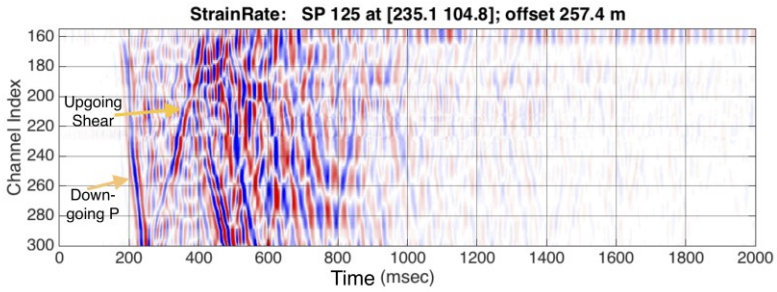

b)

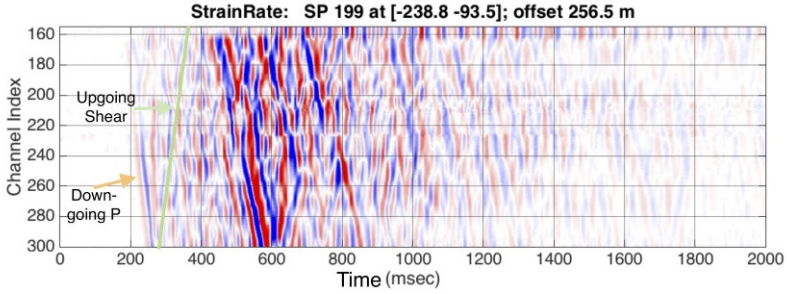

Figure 3: DASV data depth vs. time for 2 shots at 257m and 256 offset respectively a) Shot point 30125. Downgoing p-wave, upgoing (reflected/converted) s-wave. b) Shot point 199. Downgoing p-wave with weaker upgoing (reflected/converted) s-wave (figure courtesy of D. Miller, details in Miller, 2018)

This paper describes the methods used to probe the DASV data for information on the important faults of Brady's. As seen in the figure above, the DASV data is ripe with mode conversions. Migration methods are capable of simulating wave propagation in complex earth models, thus accounting for scattering and mode conversions. We use reverse time migration and the Siler and Faulds' fault model (2013) as reflectivity to begin to explain the DASV signals in terms of the geothermal reservoir faulting.

1.2 Reverse time migration: advantages and disadvantages

All migration algorithms (reverse time migration here) image single scattering events, either reflections or diffractions. These algorithms are based on the Born approximation and decompose the medium into a background model responsible for travel time (i.e. velocity), and a perturbation model responsible for the reflections and diffractions (i.e. reflectivity)(Woodward, 1992). Theoretically, with a dense grid of source and receiver offsets, there is enough azimuthal and angle coverage to see diffractions and reflections.

Often ray paths are used to approximate how seismic energy propagates and samples the subsurface, but there are shortcomings to this approximation: they don't account for complex multi-pathing, or scattering at locations of high contrast between physical properties. In contrast, wave-equation migration-based methods use the full seismic wavefield. Such methods have high computational cost that limits their applicability, but advances in computer hardware and software allow for fast processing of large volumes of data, making such methods feasible. The acoustic wave equation can be used to describe approximately the propagation of seismic waves in subsurface media. The 3D acoustic wave equation is

$$\frac{1}{v^2}\frac{\partial^2 p}{\partial t^2} = \frac{\partial^2 p}{\partial x^2} + \frac{\partial^2 p}{\partial y^2} + \frac{\partial^2 p}{\partial z^2} + f(x, y, z; t) \tag{1}$$

where *v, p, t* and *f* are the media velocity, the scalar wave field, time, and the source term, respectively, and x, y, z are spatial coordinates. Acoustic migration (simulating pressure *p*) is used in this work, not elastic migration which simulates displacement. The reflections (P to P and P to S) are kinematically created by simulating the move-out. Amplitudes are not preserved as the final image represents the zero-lag cross correlation between the source and receiver wavefields.

The migration used is a prestack depth migration algorithm called RTM (reverse time migration). It is based on the imaging principle of Claerbout (1971), where a reflector exists when source and receiver wavefields coincide in space at zero time. Pre-stack depth migration code using the whole wavefield for each source and all receiver positions will give an accurate image of the subsurface if the velocity is correct and reflections and/or diffractions are present.

RTM migrates shot gathers and uses all offsets available (from all receiver positions for a given shot): the source wavefield is forward propagated and the observed or synthetic data is backward-propagated. Both wavefields are then multiplied at each time step and summed across all time steps to form the final image. Each gather produces one partial image that is summed to all the other images (coming from all the other shots) to yield the final image. It is called a "shot profile" algorithm, because it migrates shot gathers as opposed to Kirchhoff migration, which is trace-based and doesn't account for sorting. All results presented in this paper are illumination-compensated, such that the image is divided by illumination, increasing reflectivity where illumination is low boosting deeper events (reflectors).

1.3 Velocity model used

As described in Section 1.2, RTM will be highly influenced by the velocity model used. Imaging is best performed with body waves which are generated by the vibroseis truck. We use P-wave (Vp) and S-wave (Vs) velocities estimated from sweep interferometry recorded during the March 2016 experiment (Matzel et al., 2017) to image converted-wave reflections generated by the vertical vibrator (assumed a P-wave source). Most figures in this paper will use the flattened cube convention of Figure 4a, which contains the depth slice (top), inline (bottom left, PoroTomoX constant), and cross-line (bottom right, PoroTomoY constant).

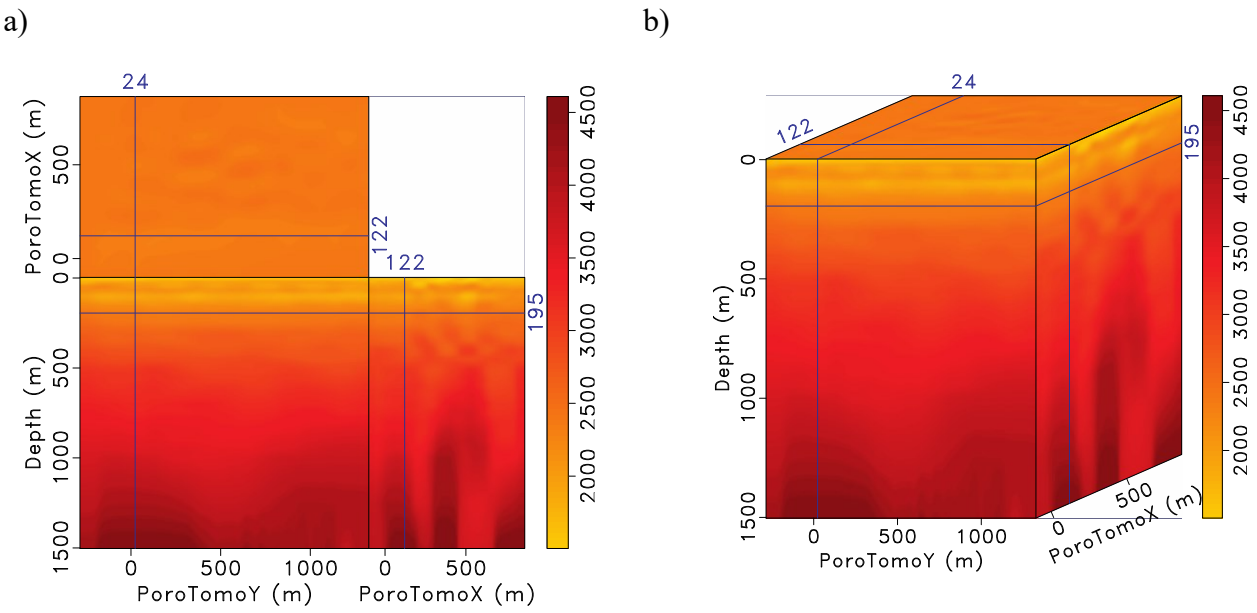

Figure 4: P-Wave Velocity (Vp) model from sweep interferometry (Matzel et al., 2017) **with the black lines approximately indicating the location of Well 56-1 at PoroTomoY=119, PoroTomoX=24, and depth is 195m. a) the flattened cube view with the top the depth slice at 195 meters below reference elevation of 1,277m above WGS84 ellipsoid, the lower left the PoroTomoX=122 slice (inline), the lower right the PoroTomoY=24 slice (cross-line) b) is the 3D perspective**

Velocity uncertainty is one of the factors that reduces the ability of RTM to accurately image the location of the faults. Figure 5 shows P-wave interval velocity versus depth estimates at the location of Well 56-1(Matzel et al., 2017; Feigl et al., 2017; Thurber et al., 2017; Feigl and Team, 2018) and the interval velocity obtained directly from the DASV data (Miller and Coleman, 2018).

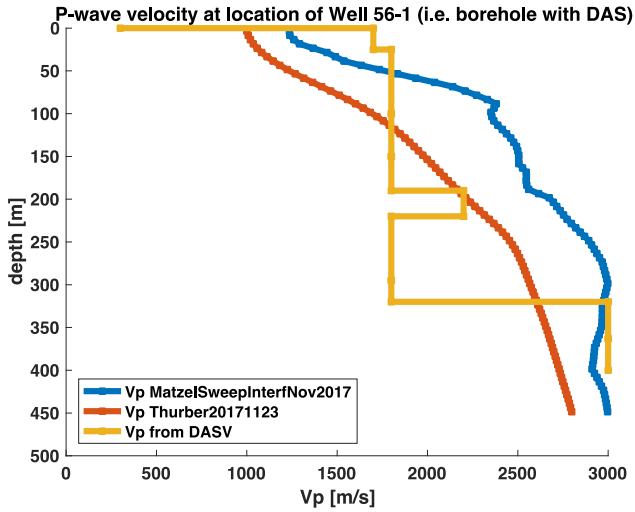

Figure 5: Different P-wave velocities deduced from sweep interferometry (Matzel et al., 2017)**, body-wave tomography** (Thurber et al., 2017) **and directly from DASV data** (Miller and Coleman, 2018)**.**

2. ESTIMATING ILLUMINATION VOLUME: SYNTHETIC MODELING

To understand its limitations through modeling and imaging, synthetic data given the Brady's experiment acquisition geometry were generated, and then migrated to isolate our geometry limitations from noise sources and poor coupling. Noise in the data (ground roll, statics/near surface problems, ambient noise, etc.) and an erroneous velocity model will affect the migration results. Also, if the data coverage is not adequate, resulting in a poor illumination of the subsurface, migrated images will be affected as well. The synthetic modeling will allow for analyzing if the acquisition geometry allows for illumination of the major faults and events of interest.

2.1 Four horizontal reflectors (PP & PS)

The first synthetic test consists of four horizontal reflectors (two constant velocity layers) that extend at depths 750m, 900m, 1,150m and 1,300m respectively (see Figure 6b) to demonstrate how much of the image is reliable given the reflection-point illumination coverage (where illumination describes the degree to which the source energy explores the model space). Given the geometry of the sources, certain areas will not be probed by the vibe energy, and thus migration artifacts will dominate. The current velocity model for the area (Figure 4) will also affect the image, and therefore is used in this modeling exercise.

Figure 6 contains the two RTM images (a and c) and the model containing the 4 reflectors (b). Figure 6a is the imaging result using the p-wave velocity for the down and up-going, referred to as the P-P image. Figure 6c is the imaging result using the p-wave velocity for the down-going energy and the shear-wave velocity for the upgoing, referred to as the P-S image. RTM images are composed of a relative reflectivity, where both white and black are stronger magnitudes in images presented in this paper. Experienced interpreters look for and identify coherent structures or events in these images. For example, in Figure 6a and c we see the horizontal reflectors at locations that straddle the well location (about +/-400m in Y and +/-300m in X). Beyond this, the image "structure" changes to a "migration smile" indicating poor illumination in that location of the model in these areas.

Thus, given the approximately 130 meters of reliable fiber in the well and the shotpoint geometry, an 800m (PoroTomoY) by 600m (PoroTomoX) by 500m (depth) volume can successfully recover the four horizontal reflectors. The depth cross section (Figure 6a) shows how the most sensitivity is northeast of the well: the larger swath of darker color in the depth slice (top) indicates the qualitative reflectivity (image) divided by the illumination. These results indicate that a doublet (reflection from the contrast of *both* the top and bottom of the reflectors) may be observed. Figure 6c (P-S image) reduces the illumination in the depth slice, but it appears to increase the recovery of the deeper flat reflector (at 1,100m depth). Thus, this final reflectivity model indicates a general volume where we can trust features to be possible subsurface structure and not migration artifacts.

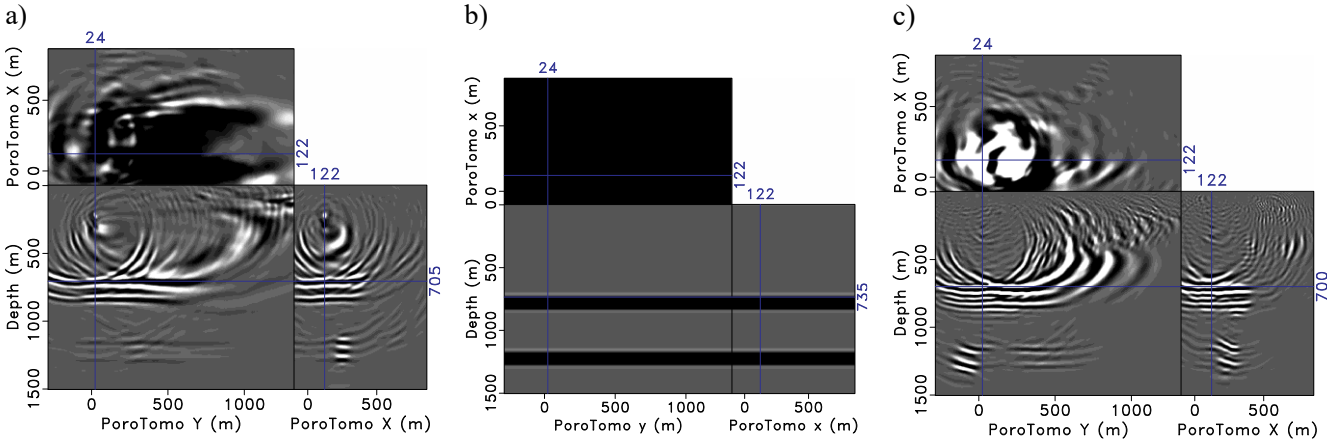

Figure 6: RTM result from two flat layers (four reflectors) at 700 and 1100m depth. a) P-P imaging b) the reflectors c) P-S imaging

3. DATA GENERATION OF 5 FAULT MODEL

Next, forward modeling of the data and imaging was performed using the same velocity model and the current fault model of Brady's (Figure 2) as a reflectivity contrast to analyze if certain fault dips and strikes would be detectable given the shot geometry. First we compare the data generated from this combination of the velocity model (Matzel et al., 2017) and fault reflectivity (from Siler and Faulds, 2013) to the observed data for shots 30125 (3 indicates stage 3, and 125 the location), the same shots shown in Figure 3. Before describing the observed and synthetic data, Figure 7 presents the faults at the inline and cross-line sections of the coordinates for shot 30125: the source location is at the black lines, and the x location of the DAS fiber is drawn with the yellow line. The steeply dipping faults provide the angles for mode conversions: p-wave to shear waves as observed in the data. It is important to keep in mind that the vertical DAS fiber will be sensitive to particle motion that is parallel to the fiber, thus vertical. This will be possible from shear waves that are propagate across the cable approximately horizontally, and also expected from compressional p-waves propagating vertically.

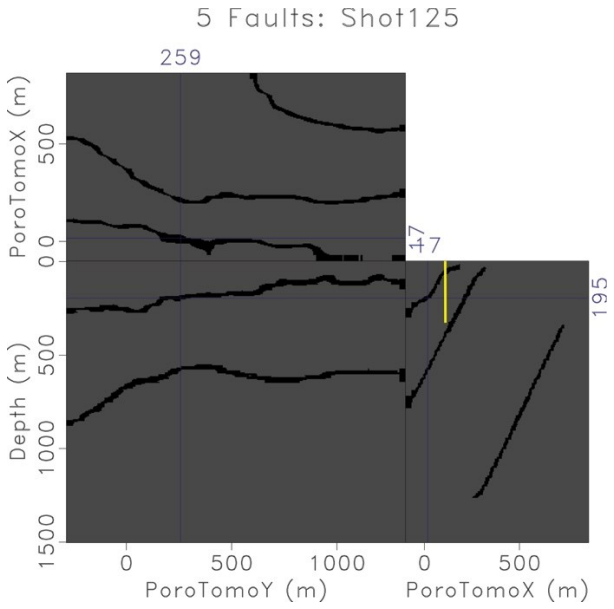

Figure 7: Fault reflectivity model at vibe point 125 (PoroTomoY=259 and PoroTomoX=17). The vertical DAS fiber in Well 56-1 is shown in yellow (PoroTomoY=24 and PoroTomoX=122).

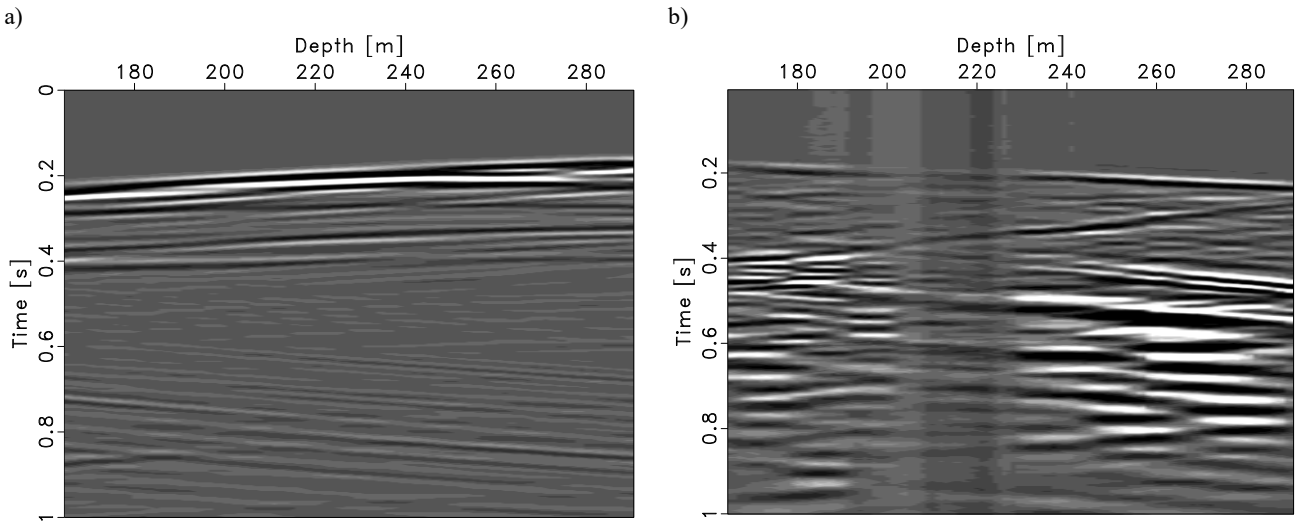

Figure 8: Vibe point 30125: a) synthetic P-S data via Born approximation/modeling and reflectivity of the 5 fault model (Siler and Faulds, 2013) and b) observed data.

Figure 8 shows the observed field data (right) and the synthetic data (left, upgoing only) for shot 30125; note that axes of Figure 8 are transposed relative to Figure 3. The Born approximation only models single scattering events (Woodward, 1992); thus, we are not able to match the first arrival that has a "negative" slope: events arriving later at deeper depths. In Figure 8b, the converted up-going s-wave is quite clearly observed as the relative moveout contrast from that of the downgoing P-wave first arrival. For this reason, the shear wave velocity was used for up-going waves, hence the notation P-S data. The opposite polarity is not possible to observe in Figure 8a since only the up-going S wave is simulated. The synthetic data follow the observed data where two events travel from the bottom up to 160m depth, arriving at approximately 0.22 and 0.4 seconds respectively.

Another feature of the observed data is the faster layer at 190m to 210m depth, where the slope of the arrivals change (Figure 8b). This is not reflected in the 3d velocity model, but well observed in many azimuths of the data. Queen et al. (2016) describe and depict in their model how this can be explained at Brady's as older, faster fault blocks that have been placed above younger, slow material.

4. REVERSE TIME MIGRATION: 5-FAULT REFLECTIVITY MODEL & BRADY'S DATA

Both the observed field signals and the synthetic from the vertical DAS fiber will be migrated, keeping in mind there are many challenges in the Brady's data: reverberating fiber (as it is not affixed to casing or tubing), multiple interfering events, etc. Ideally, the data would be further processed to isolate events of interest. Since these data unprocessed, noisier migrated images will be obtained that are more difficult to interpret than the synthetics. Another factor, which is true of both the synthetic and real data case, is the sparse shot geometry. A denser shotpoint coverage would produce cleaner migrated images by stacking out artifacts. However, we can utilize the synthetic modeling results to isolate geometry or velocity effects and attempt to distinguish migration artifacts from true geologic structures.

Two types of RTM were investigated: P-P (p-wave velocity for both up and down going waves) and P-S (p-wave velocity for up and S-wave velocity for down going waves). Upgoing shear waves are important if they cross the vertical DAS at an approximately perpendicular angle, since the DAS fiber is sensitive to vertical particle motion.

Figure 9 contains two flattened cubes that used the P-P kinematics to produce the reflectivity images (reflectivity divided by illumination) for locations at PoroTomoY=124m, PoroTomoX=672m, and depth=420m, about 560m laterally and 210m deeper from the locations shown in Figures 4 and 6. The Figure 9a contains the RTM result using the synthetic data, while Figure 9b is from the Brady's field data. These flattened cubes focus on the deepest of the three northwestern-dipping (negative PoroTomoX direction) faults (Figure 2). The intersection of the slices is approximately Northeast (positive PoroTomoXY and PoroTomoX direction) of Well 56-1.

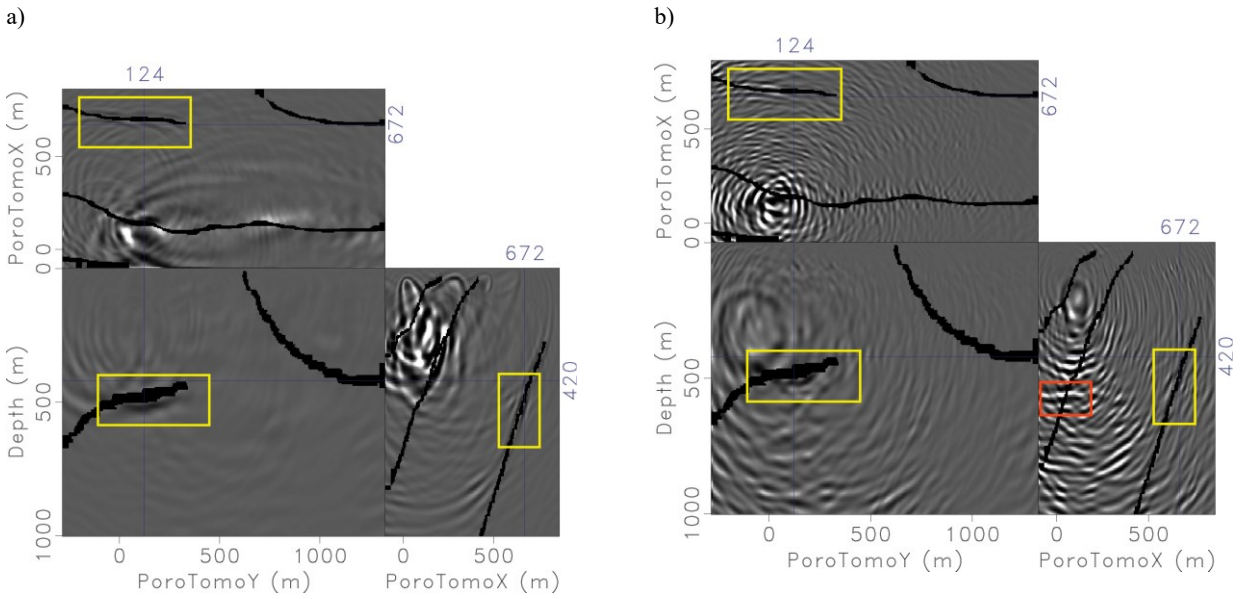

Figure 9: Deepest West-dipping Fault. Kinematics: P-wave Velocity Down & Up (P-P image) of a) synthetic 5 fault model and b) the Brady's field data

The yellow boxes highlight coherent events that coincide in both the fault model and Brady's images. All three yellow boxes are on the deepest of the three western-dipping faults. The bottom two slices demonstrate how the fault can be seen from depth ranges of 450 - 500m. Additionally, there is a possible coherent event in the Brady's data that doesn't coincide with a fault included in the synthetic modeling. This is highlighted in red in the PoroTomoX slice.

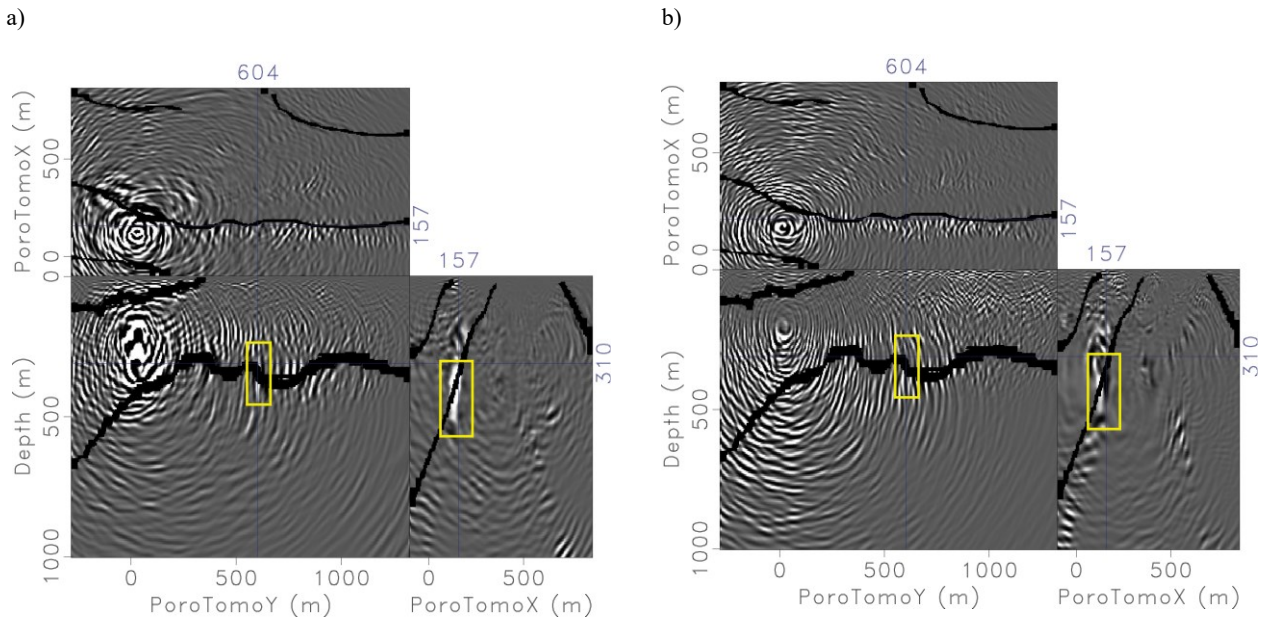

Figure 10: Middle West-dipping fault. Kinematics: P-wave Velocity Down & Shear Wave Up (P-S image) of a) synthetic 5 fault model and b) the Brady's field data

Figure 10 contains the P-S images for both the synthetic 5-fault model (left) and the Brady's field data (right). The location of these slices is PoroTomoY=604, PoroTomoX=157 and depth=310m, focusing on the middle, Western-dipping fault. Compared with Figure 9, it is about 700m Northwest and 110m shallower and is about 580m North of Well 56-1). The three yellow boxes highlight the most promising features, the middle West-dipping fault. In the crossline slice (lower right), the fault demonstrates a long from in both Figure 10a and Figure 10b. The middle western-dipping fault is a coherent, 200m-long feature (310 to 550m depth) for both the synthetic and Brady's image in the PoroTomoX slices (lower right). From probing the 3D cubes, it was discovered that this fault is well image for 400m along strike.

In the depth slice (upper left) of both images in Figure 10, the focusing effect of the velocity model is seen in just neighboring the middle West-dipping fault (see Figure 4 for the general patterns of the velocity). Focusing is also seen in the PoroTomoX and PoroTomoY panels. In the lower right panels, there are brighter spots that begin PoroTomoX=500 and depth=500, which coincide with a higher (4,500m/s versus 4,000m/s) velocity structure. There are also focusing patterns below the yellow box in the lower left panels.

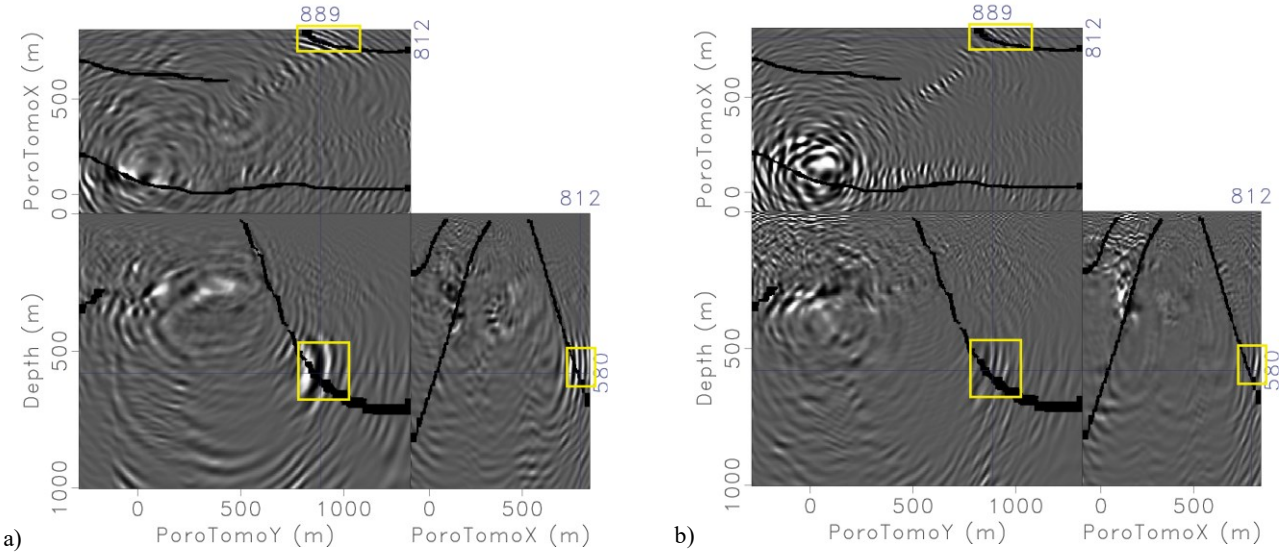

Figure 11: Far Eastern-dipping fault. Kinematics: P-wave Velocity Down & Shear Wave Up (P-S image), deeper & further Southeast from Figure 10. a) synthetic 5 fault model and b) the Brady's field data

Figure 11 is another flattened cube of the P-S results; the depth slice is almost 300m deeper, the PoroTomoY slice is about 650m East and the PoroTomoX slice is almost 300m North of Figure 10. The far Eastern-dipping fault is highlighted in the three yellow boxes. In the PoroTomoY slice there appears to be a bright spot in the eastern-dipping fault where the dip-angle is dramatically changing from steep to flat. The depth slice also shows potential for picking up the very top of the deepest of the three Western-dipping faults. This is encouraging considering it is at farthest distance from the receivers and quite deep at 580m.

4.1 Discussion

The deepest features resolved from the field data are around 600m. To improve the DAS imaging results, data should be better processed to extract as much signal as possible, and the p- and s- wave velocity model should be improved as well. That will help any depth migration algorithm. At the end of the day, we are limited by the data quality and the acquisition geometry, which influence the velocity model estimation step and the final migrated image. For example, a Radon transform could be used to filter out unwanted events in the data.

Because of Well 56-1 relative position to all the vibe points, it is very difficult to resolve any faults in the PoroTomoY plane that are close to or west of well location (PoroTomo X < 125). The results could be argument for compressive sensing to help design acquisition geometry, especially when dealing with limited budget and/or restrictions such as fumaroles and permitting, which PoroTomo was with the Emigrant Trail (Feigl et al., 2017). Compressive sensing exploits the fact that a small and carefully selected set of measurements of a compressible signal carries enough information for reconstruction and processing (Allegar et al., 2017).

5. CONCLUSIONS

It was confirmed given approximately 130 meters (with 10 meter gauge length) of reliable fiber in the well and the geometry of the vibe shots, a 800 by 600 by 500m (depth) volume can successfully recover the 2 horizontal layers (four reflectors).

The P-P images show promise for identifying the deepest of Western-dipping fault (Figure 9), and the P-S images discern the middle of the Western-dipping and the far Eastern-dipping faults of Brady's Natural Laboratory. The different angles of incidence due to the vibe shots, depth of DAS cable and dip of the faults allow for the P-S images to pick up the northeast-dipping and two deeper, western-dipping faults. Specifically, the middle of the three western faults is imaged for over 300 meters along strike (Figure 10 and Figure 11).

It is remarkable but not unheard of that the unattached, hanging DAS fiber is able to recover usable signal. Lindsey et al. (2017) describe how a variety of earthquakes are detectable using fiber deployed in standard telecommunications conduits, which are imperfectly coupled to the subsurface.

5.1 Future work

We intend to combine the efforts to image with the vertical and horizontal DAS and geophones. Jreij et al. (2018) describes how these different sensors have their own unique sensitivities to different wave modes and different offsets. Combining these data could improve accuracy of imaging efforts to identifying scattering events. Additionally, test should be run using a layer cake velocity model to more

thoroughly investigate velocity focusing affects. Currently work is being done to use these images and the a priori information on the fault locations to determine the value of information (VOI) of the different seismic sensors (Jreij et al., 2018).

A more thorough analysis of the wavefields used during the imaging process with RTM may provide some angles of reflection, thus insight into the mode conversions by confirming the angles of incidence for the shot sources and faults(Rickett and Sava, 2002). With angles of incidence, we may be able to explain where to P to S mode conversions occur via Zoeppritz equations.

Lastly, after these analyses are done, other stages (different shot times) could be processed and imaged, to evaluate if any 4D changes are detectable: pumping and injection activities are believed to have affected the saturation in shallow subsurface. This may change some of the Thomsen parameters that are fluid indicators (e.g. incompressibility).

REFERENCES

Allegar, N., Herrmann, F.J., and Mosher, C.C., 2017, Introduction to this special section: Impact of compressive sensing on seismic data acquisition and processing: The Leading Edge, v. 36, p. 640–640, doi: 10.1190/tle36080640.1.

Claerbout, J., 1971, Toward a unified theory of reflector mapping: Geophysics, v. 36, p. 467–481.

Coolbaugh, M.F., Sladek, C., Kratt, C., and Edmondo, G., 2004, Digital mapping of structurally controlled geothermal features with GPS units and pocket computers: Geothermal Resources Council Transactions, v. 28, p. 321–325.

Daley, T.M., Miller, D.E., Dodds, K., Cook, P., and Freifeld, B.M., 2016, Field testing of modular borehole monitoring with simultaneous distributed acoustic sensing and geophone vertical seismic profiles at Citronelle, Alabama: Geophysical Prospecting, v. 64, p. 1318–1334, doi: 10.1111/1365-2478.12324.

Faulds, J.E., Coolbaugh, M.F., Benoit, D., Oppliger, G., Perkins, M., Moeck, I., and Drakos, P., 2010, Structural Controls of Geothermal Activity in the Northern Hot Springs Mountains, Western Nevada: The Tale of Three Geothermal Systems (Brady's, Desert Peak, and Desert Queen): Geothermal Resources Council Transactions, v. 34, p. 675–683.

Feigl, K.L., Lancelle, C., Lim, D.D., Parker, L., Reinisch, E.C., Ali, S.T., Fratta, D., Thurber, C.H., Wang, H.F., Robertson, M., Coleman, T., Miller, D.E., Lopeman, J., Spielman, P., et al., 2017, Overview and Preliminary Results from the PoroTomo project at Brady Hot Springs, Nevada: Poroelastic Tomography by Adjoint Inverse Modeling of Data from Seismology, Geodesy, and Hydrology, *in* PROCEEDINGS, 42nd Workshop on Geothermal Reservoir Engineering, Stanford, California, p. 1–15.

Feigl, K., and Team, P., 2018, Overview and Preliminary Results from the PoroTomo project at Brady Hot Springs, Nevada: Poroelastic Tomography by Adjoint Inverse Modeling of Data from Seismology, Geodesy, and Hydrology, *in* Stanford Geothermal Workshop,.

Jreij, S., Trainor-Guitton, W., and Simmons, J., 2018, Improving Point-Sensor Image Resolution with Distributed Acoustic Sensing at Brady's Enhanced Geothermal System, *in* Stanford Geothermal Workshop,.

Lindsey, N.J., Martin, E.R., Dreger, D.S., Freifeld, B., Cole, S., James, S.R., Biondi, B.L., and Ajo-Franklin, J.B., 2017, Fiber-Optic Network Observations of Earthquake Wavefields: Geophysical Research Letters, v. 44, p. 11,792-11,799, doi: 10.1002/2017GL075722.

Mateeva, A., Lopez, J., Potters, H., Mestayer, J., Cox, B., Kiyashchenko, D., Wills, P., Grandi, S., Hornman, K., Kuvshinov, B., Berlang, W., Yang, Z., and Detomo, R., 2014, Distributed acoustic sensing for reservoir monitoring with vertical seismic profiling: v. 62, p. 679–692, doi: 10.1111/1365-2478.12116.

Matzel, E., Zeng, X., Thurber, C., Luo, Y., and Morency, C., 2017, Seismic Interferometry Using the Dense Array at the Brady Geothermal Field, *in* 42nd Stanford Geothermal Workshop on Geothermal Reservoir Engineering, p. 3–6.

Miller, D.E., and Coleman, T., 2018, DAS and DTS at BradyHot Springs: Observations about Coupling and Coupled Interpretations, *in* Stanford Geothermal Workshop,.

Queen, J.H., Daley, T.M., Majer, E.L., Nihei, K.T., Siler, D.L., and Faulds, J.E., 2016, Surface Reflection Seismic and Vertical Seismic Profile at Brady ' s Hot Springs , NV , USA: 41st Workshop on Geothermal Reservoir Engineering, p. SGP-TR-209.

Raterman, K.T., Farrell, H.E., Mora, O.S., Janssen, A.L., Gomez, G.A., Busetti, S., Mcewen, J., Davidson, M., Friehauf, K., Rutherford, J., Reid, R., Jin, G., Roy, B., and Warren, M., 2017, Sampling a Stimulated Rock Volume: An Eagle Ford Example: , p. 24–26, doi: 10.15530/urtec-20172670034.

Rickett, J., and Sava, P.C., 2002, Offset and angle-domain common image-point gathers for shot-profile migration: Geophysics, v. 67, p. 883–889.

Siler, D.L., and Faulds, J.E., 2013, Three-Dimensional Geothermal Fairway Mapping : Examples From the Western Great Basin , USA: GRC Transactions, v. 37, p. 327–332.

Thurber, C., Zeng, X., Parker, L., Lord, N., Fratta, D., Wang, H., Matzel, E.M., Robertson, M., Feigl, K.L., and PoroTomo Team, 2017, Active-Source Seismic Tomography at Bradys Geothermal Field, Nevada, with Dense Nodal and Fiber-Optic Seismic Arrays, *in* Fall Meeting American Geophysical Union, New Orleans.,.

Woodward, M.J., 1992, Wave-equation tomography: Geophysics, v. 57, p. 15–26.